Int. J. Heat Mass Transfer. Vol. 33, No. 10, pp. 2329–2344, 1990
Printed in Great Britain

0017–9310/90 $3.00 + 0.00

Thermal and fluid flow instabilities in buoyancy-driven flows in open-ended cavities

KAMBIZ VAFAI and JAVAD ETTEFAGH
Department of Mechanical Engineering, The Ohio State University, Columbus, OH 43210, U.S.A.

(*Received* 21 *September* 1989 *and in final form* 24 *January* 1990)

Abstract—The basic features of the buoyancy-driven convection in an open-ended cavity are analyzed and an in depth presentation of the related results are given in this work. It is shown that, at higher Rayleigh numbers, a one to one relationship exists between the frequency of the periodic oscillations in the Nusselt number and the central vortex's oscillations and location inside the cavity. In fact, for any given type of oscillatory pattern (e.g. asymmetric sinusoidal or distorted W), the frequency of the oscillations of the Nusselt number (or the central vortex inside the cavity) increases linearly as the Rayleigh number increases. For air, this linear relationship was explicitly determined. Furthermore, it is determined that, for cases which $Ra \geqslant 9 \times 10^5$, the central vortex's oscillation frequency and/or amplitude becomes much higher and it starts to deviate from any type of repeatable pattern. It is proposed that it is this irregular high frequency and/or amplitude of the central vortex coupled with the flow separation around the mid-section of the lower block that triggers the transition to turbulent flow.

1. INTRODUCTION

ONE OF the main characteristics of the buoyancy induced flows in the open-ended cavities is its basic geometry. This is because several, complex geometries, such as the brake housing of an aircraft, can be approximated or constructed from this basic geometry. Problems involving natural convection in open cavities were studied by Doria [1] in predicting fire spread in a room and by Jacobs *et al.* [2, 3] in modeling circulation above city streets and geothermal reservoirs. Chan and Tien [4, 5] studied natural convection in a shallow open cavity using laser Doppler velocimetry in which their conclusion about the open boundary condition was that the outgoing flow is force driven by the open cavity heating while the incoming flow is affected by the external conditions. Experimental studies were also done by Humphrey and co-workers [6] and Sernas and Kyriakides [7], in modeling solar receivers. By focusing on this basic geometry, a better understanding of the flow characteristics around a sharp corner and its crucial importance in directly influencing the fluid mechanics of the near field will be achieved. In the present study the transient, two-dimensional buoyancy-driven flow in open-ended cavities is analyzed. The effects of sharp corners on vorticity generation and the flow instabilities are discussed. The importance of the far field boundary conditions and the interaction between the controlling variables are all discussed and in-depth analysis of the fluid flow and vortex interaction in the open-ended cavity is presented. For example it is found that, the flow and heat transfer characteristics inside the open-ended cavity and in its immediate surroundings are affected by a much larger computational domain of influence than what has been used by previous investigators. Although a few authors have obtained their steady state results through transient solution of the governing equations, reports on transient results for the open cavity configuration are very rare in literature. For example, graphical presentation of the cavity Nusselt number vs time (for only a very short time period) by Penot [8] is among the very limited transient results available in the literature.

In the present study, the transient characteristics of the flow field including the heat transfer characteristics inside an open-ended cavity and near the openings are thoroughly researched. The transient behavior of the flow field is characterized by the secondary recirculating flow formation along the lower block in addition to the primary flow inside the open-ended cavity. The complete time history of the flow development inside the open-ended cavities consisting of the interactions between the secondary recirculating flow and the primary flow has been analyzed in this paper. It is found that the time history development of the flow includes the secondary recirculating flow formation, and the rise in the strength of this recirculating flow to a maximum value. After that, this recirculating flow continues to lose its strength until it completely disappears from the flow field (the approach towards the steady state). The transient Nusselt number which represents the heat transfer process is shown to exhibit an overshooting followed by damped oscillations around its steady state value. It is rigorously proved that a one to one relationship exists between the frequency of oscillations in the Nusselt number and the central vortex's oscillations (the central vortex is discussed in detail later) and location inside the cavity and that in fact, these oscillations are linearly dependent on the Rayleigh

NOMENCLATURE

d	length of the cavity [m]
H	open cavity height [m]
Nu_c	Nusselt number for the cavity
Pr	Prandtl number, ν/α
Ra	Rayleigh number, $g\beta H^3\Delta T/\alpha\nu$
T	temperature [K]
u	non-dimensionalized x-component velocity
v	non-dimensionalized y-component velocity
x	non-dimensionalized horizontal coordinate
y	non-dimensionalized vertical coordinate.

Greek symbols

α	thermal diffusivity [$m^2 s^{-1}$]
β	thermal expansion coefficient of fluid [K^{-1}]
ζ	vorticity
θ	dimensionless temperature
μ	dynamic viscosity [$kg\ m^{-1} s^{-1}$]
ν	kinematic viscosity [$m^2 s^{-1}$]
ρ	fluid density [$kg\ m^{-3}$]
ψ	stream function.

Subscripts

1	lower block
2	upper block
min	minimum value
max	maximum value
∞	free stream.

cal experiments it becomes clear that, for cases which $Ra \geqslant 9\times 10^5$, the central vortex's oscillation frequency and/or amplitude becomes much higher and it starts to deviate from any type of repeatable pattern. Based on the facts mentioned earlier it is then proposed that it is this irregular high frequency movement of the central vortex coupled with the flow separation around the mid-section of the lower block that triggers the transition to turbulent flow.

2. FORMULATION AND NUMERICAL SCHEME

The two-dimensional open-ended cavity which is analyzed in this work is shown in Fig. 1. The lower block and upper block temperatures of the slot are at constant temperatures T_1 and T_2 and the length and the height of the cavity are d and H, respectively. The vertical portions of both blocks are assumed to be adiabatic and the surrounding fluid communicating with the open-ended cavity is at an ambient temperature T_∞. The transformed governing equations in terms of vorticity, stream function, and temperature are

$$\nabla^2\psi = \zeta$$

$$\frac{\partial\zeta}{\partial t}+u\frac{\partial\zeta}{\partial x}+v\frac{\partial\zeta}{\partial y} = Pr\cdot\nabla^2\zeta - Pr\cdot Ra\cdot\frac{\partial\theta}{\partial x}$$

$$\frac{\partial\theta}{\partial t}+u\frac{\partial\theta}{\partial x}+v\frac{\partial\theta}{\partial y} = \nabla^2\theta$$

where

$$\zeta = \frac{\partial u}{\partial y}-\frac{\partial v}{\partial x},\quad u=\frac{\partial\psi}{\partial y},\quad v=-\frac{\partial\psi}{\partial x}$$

and

$$Ra=\frac{g\beta H^3\Delta T}{\alpha\nu},\quad Pr=\frac{\nu}{\alpha},\quad A=H/d.$$

In the above expressions Ra is the Rayleigh number, Pr the Prandtl number, A the aspect ratio, g the gravitational acceleration, α the thermal diffusivity of the medium, β the coefficient of volume expansion, and ν the kinematic viscosity of the fluid medium. The above equations were nondimensionalized by using the open cavity height, H, H^2/α, (T_1-T_∞), and α/H as characteristic length, time, temperature difference, and velocity, respectively.

The rate of heat transfer across the open-ended cavity was computed in terms of a cavity Nusselt number which represents the non-dimensional total rate of heat transfer from the entire cavity, and is given as

$$Nu_c = -A\int_0^{1/2}\left.\frac{\partial\theta}{\partial y}\right|_{y=-A/2}dx+\frac{A}{\theta_2}\int_0^{1/2}\left.\frac{\partial\theta}{\partial y}\right|_{y=A/2}dx.$$

To reduce the size of the computational domain, the

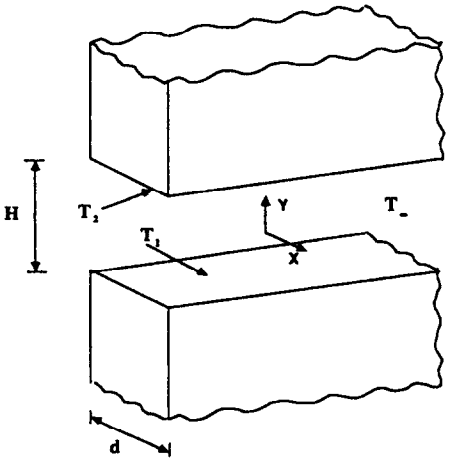

FIG. 1. Schematic of an open-ended cavity.

expected symmetry condition was used at the centerline of the open-ended cavity (see the Appendix). The validity of using the symmetry conditions at the centerline of the cavity was checked through a series of numerical runs. The non-uniform grid network used in this work possesses a *very fine* grid structure near the symmetry line which gradually converts to a *fine* grid structure inside the cavity. In the extended computational domain, the grid distribution is fine near the vertical portions of the cavity and then it gradually becomes coarser towards the far field. In this work the grid distribution was chosen such that the following criteria:

$$\Delta x_i - \Delta x_{i-1} = O\{(\Delta x_{i-1})^2\}$$

and

$$\Delta y_j - \Delta y_{j-1} = O\{(\Delta y_{j-1})^2\}$$

would always be satisfied. In the above expressions Δx_i and Δy_j are the spatial distances between nodal locations x_i and x_{i+1}, and y_j and y_{j+1}, respectively. Satisfaction of the above criteria ensured that we would not experience any extra loss of accuracy resulting from the usage of a variable grid system. In our numerical simulations the fluid was assumed to be initially at rest and at the ambient temperature. Aside from being quite basic, the initial conditions were motivated by physical considerations as they prevail in a variety of practical problems. By performing a series of separate runs, using different initial conditions it was ascertained that the initial conditions do not have any influence on the regular steady state results.

At each time step, the elliptic equation (Poisson equation) is solved by an extrapolated Jacobi scheme, an iterative method with optimum over-relaxation. This scheme has some similarities with the original Jacobi scheme [9]. However, in this scheme at iteration level κ only half of the nodal points are updated. At the next iteration level, $\kappa+1$, the other half of the nodal points are updated and the process continues on like this. Furthermore, before starting each iteration the newly iterated nodal values, $\phi_{i,j}^{\kappa+1}$ are over-relaxed using the optimum over-relaxation parameter.

It can be shown that this method has the same convergence rate as the conventional SOR method and even its spectral radius is the same as that of SOR. Hence, the algorithm for its optimum over-relaxation parameter is the same as the one for SOR. But, its advantage is that it can be vectorized, which makes it more efficient when used on a Cray [9]. This efficiency is best explained when one realizes that most of the computer time spent is resulting from the solution of the Poisson equation. The basic method used for the two transport equations at the interior points is as follows. The energy equation is advanced in time according to the ADI method. The spatial derivatives are approximated in the non-uniform grid system ($x_{i+1}-x_i=\Delta x_i$, $y_{j+1}-y_j=\Delta y_j$) by central differences in the following form:

$$\left(\frac{\partial\theta}{\partial x}\right)_{i,j} = \frac{\theta_{i+1,j}-\theta_{i-1,j}}{\Delta x_i+\Delta x_{i-1}} \tag{1}$$

$$\left(\frac{\partial^2\theta}{\partial x^2}\right)_{i,j} = 2\frac{\Delta x_{i-1}\theta_{i+1,j}-(\Delta x_i+\Delta x_{i-1})\theta_{ij}+\Delta x_i\theta_{i-1,j}}{\Delta x_i\Delta x_{i-1}(\Delta x_i+\Delta x_{i-1})}. \tag{2}$$

Since our grid distribution was chosen such that $\Delta x_i-\Delta x_{i-1}=O\{(\Delta x_{i-1})^2\}$, then the use of equation (1) or an expression which is based on three point differencing for $(\partial\theta/\partial x)_{i,j}$ will produce a truncation error which would be locally of the same order of magnitude as that which would occur in a uniformly spaced grid system. The advection terms are represented by the second upwind differencing to avoid the stability problems associated with central differencing and the inaccuracies caused by the artificial viscosity effect associated with the first-order upwind differencing. In this type of differencing which is called the 'Donor cell' method [10], some sort of average interface velocities on each side of the considered mesh point are defined. The sign of these velocities determined by central differencing, specifies which cell values of the field function should be used. This method can easily be interpreted from the control volume point of view, with interface velocities determined by averaging and interface field variable values determined by the flow direction. The above procedure can be combined into a single expression which is easily implemented in our solution algorithm

$$\left(u\frac{\partial\theta}{\partial x}\right)_{i,j} = \frac{\begin{aligned}[(u_R-|u_R|)\theta_{i+1,j}+(u_R+|u_R|\\ -u_L+|u_L|)\theta_{i,j}-(u_L+|u_L|)\theta_{i-1,j}]\end{aligned}}{\Delta x_i+\Delta x_{i-1}} \tag{3}$$

where

$$u_R = \frac{u_{i,j}+u_{i+1,j}}{2}, \quad u_L = \frac{u_{i-1,j}+u_{i,j}}{2}.$$

It is assumed that the steady state conditions have been reached when the following convergence criteria:

$$\frac{\phi_{i,j}^{n+1}-\phi_{i,j}^{n}}{\phi_{i,j}^{n+1}} \leqslant 10^{-3}$$

for temperature, stream function, and vorticity have been met. In the above expression, n refers to any particular time level and ϕ represents either one of the three dependent variables.

A part of this study involves the development of realistic, accurate and stable boundary conditions. The no-slip boundary condition appears at the block surfaces, along which the value of the stream function is constant, in which the constant is chosen to be zero. The vorticity is determined in the customary manner, by expanding the stream function out from the walls in a Taylor series and invoking the no-slip condition. Temperature conditions are specified temperature at the base and adiabatic conditions at the vertical portion of the blocks. At the centerline, the symmetry

Table 1. Different choices which were analyzed for representing the far field boundary conditions

Variable	Choice I	Choice II	Choice III
ψ	Const.	$\partial\psi/\partial n = 0$	$\partial^2\psi/\partial n^2 = 0$
θ	Const.	$\partial\theta/\partial n = 0$	$\partial^2\theta/\partial n^2 = 0$
ζ	Determined from the ψ information		

requires that the vorticity, stream function, and the horizontal temperature gradient be zero. The open boundary conditions are specified by setting the normal gradients of the velocity and the temperature to zero. The vorticity values at these boundaries are calculated from the stream function distribution. Due to an implicit method applied to the vorticity transport equation, it is necessary to temporarily assume the vorticity distribution on the boundaries at times $n+1/2$ and $n+1$ equal to that at time n. Thus, the boundary vorticity is out of step with the advancement of the interior vorticity field. The error introduced by this assumption is very small and can be even further reduced by choosing small time steps. Furthermore, the error completely diminishes by the approach towards steady state. However, it should be noted that the stream function and temperature fields were determined by an implicit routine which simultaneously incorporated the boundary and the internal points into the solution algorithm at each time step. In the course of our work we had analyzed several different expressions summarized in Table 1, as possible candidates for representing the far field boundary conditions.

In Table 1, n denotes the normal direction with respect to any of the far field boundary lines. All the boundary conditions given in Table 1 were chosen such that they could be directly incorporated into the stream function and the energy equations. This way the stream function and the temperature fields were determined using an implicit routine which simultaneously incorporated the boundary and the internal points into the solution algorithm at each time step thus, creating a very accurate and stable algorithm. To the authors' knowledge, only the use of the above-mentioned boundary conditions permit the point governing equations being satisfied identically everywhere including the boundaries through the use of an implicit routine which simultaneously incorporates the boundary and the internal points into the solution algorithm at each time step. Other types of boundary conditions suffered from two serious drawbacks. First, they required some type of extrapolation scheme, thereby reducing their accuracy. In addition, they could not be used in an implicit routine which simultaneously incorporated the boundary and the internal points into the solution algorithm at each time step. Thus, the use of any other set of expressions for the far field boundary conditions would introduce a significant degree of inaccuracies compared to using the expressions given in Table 1.

After doing extensive numerical experimentation with the above-mentioned boundary conditions we had found that the choice, $\partial^2\psi/\partial n^2 = 0$, for the stream function and the choice, $\partial\theta/\partial n = 0$, for the temperature field are, from a numerical point of view, the best choices. That is this set of boundary conditions can simulate the true conditions inside the computational domain for a lesser number of extensions. From a physical point of view, $\partial^2\psi/\partial n^2 = 0$, places the least degree of restriction on the flow field (compared to the other choices presented in Table 1). However, although, $\partial\theta/\partial n = 0$, from a physical point of view is not the least restrictive option (the least restrictive option is: $\partial^2\theta/\partial n^2 = 0$) we still found it to be the best choice with respect to simulating the true conditions inside the computational domain for a lesser number of extensions. It should be noted though, with respect to the cavity and its immediate surroundings, all the choices given in Table 1 produced the same results when the computational domain was extended far enough. Furthermore, the improvements in terms of reducing the number of extensions (by using the second or third set of outer boundary conditions given in Table 1) necessary for producing the conditions inside the computational domain were relatively insignificant. This could be attributed to the fact that all the boundary conditions given in Table 1 were chosen such that they would be implicitly and simultaneously incorporated into the solution algorithm at each time step.

3. ANALYSIS OF OSCILLATIONS IN THE TEMPORAL NUSSELT NUMBER VARIATIONS FOR HIGH RAYLEIGH NUMBERS

The transient behavior of the flow field through the formation of vortices, the formation of the stratified region, the effects of the geometric and thermophysical parameters and the influence of the Rayleigh number and different temperature levels on the flow field are discussed in another related investigation [11]. In here the concentration is directly focused on thermal and fluid flow instabilities in open-ended geometries. Figure 2 illustrates the Rayleigh number effects on transient behavior of the cavity Nusselt number. The transient response shows an overshooting of the cavity Nusselt number, followed by damped oscillations around a steady state value. Oscillations in the Nusselt number were also observed in an open-ended cavity obstructed by a porous medium [12]. As expected, the initial overshoot of the cavity Nusselt number starts earlier in time and is steeper for higher Rayleigh numbers. This is because the time that it takes to heat up the fluid particles along the lower block is decreased, resulting from steeper temperature gradients, as the Rayleigh number is increased. Furthermore, the frequency of the oscillations increases and the damping of the oscillations decreases with an increase in the Rayleigh

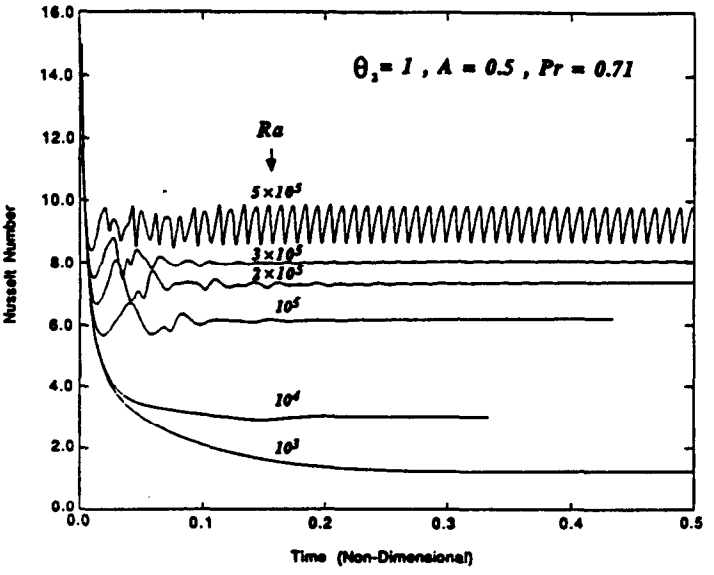

FIG. 2. Time history of the cavity Nusselt number for $\theta_2 = 1$, $A = 0.5$, $Pr = 0.71$ and $10^3 \leqslant Ra \leqslant 5 \times 10^5$.

number. The low damping effect at high Rayleigh number flows is the cause for the transition to time-dependent convection as illustrated by a periodic behavior of the cavity Nusselt number for the cases with $Ra \geqslant 3 \times 10^5$. As it can be seen, for these cases, no steady state solution exists. Therefore, for these situations if the problem would have been analyzed through a non-transient formulation, a multitude of solutions would be found depending on the initial guesses and disturbances. Of course, none of the aforementioned solutions would represent the real situation. For flows with $Ra > 9 \times 10^5$, due to an increase in the frequency of oscillations and a decrease in damping of oscillations, the flow becomes quite unstable. This situation is discussed later in more detail.

To describe these oscillations in more detail the results of the numerical runs for air ($\theta_2 = 1$, $A = 0.5$) and for $Ra = 3 \times 10^5$, 3.5×10^5, 4×10^5, 4.5×10^5, 5×10^5, 5.5×10^5, 6×10^5, 6.5×10^5, 7×10^5, 7.5×10^5, 8×10^5, and 9×10^5, will be discussed. These oscillations essentially start from $Ra \geqslant 3 \times 10^5$ (although the amplitude of oscillations for $Ra = 3 \times 10^5$ is quite small). In the range of $3 \times 10^5 \leqslant Ra \leqslant 5.5 \times 10^5$, the oscillations are in the shape of asymmetric sinusoidal waves. For values of $Ra \geqslant 6 \times 10^5$, these sinusoidal oscillations in the Nusselt number distribution will no longer exist. For Rayleigh numbers larger than $Ra = 6 \times 10^5$, the sinusoidal oscillations are converted to distorted W shaped oscillations. This latter pattern of oscillations in the temporal Nusselt number distribution will persist from $Ra > 6 \times 10^5$ to $Ra < 9 \times 10^5$. Finally, for $Ra \geqslant 9 \times 10^5$ the W shaped pattern breaks down to some intermediary W's and also part of the flow separates from the central portion of the lower block. Furthermore, on the basis of several numerical experiments it becomes clear that, for cases which $Ra \geqslant 9 \times 10^5$, the central vortex's oscillation frequency and/or amplitude (the oscillation frequency of the central vortex is discussed in detail later for $3 \times 10^5 \leqslant Ra < 9 \times 10^5$) becomes much higher and it starts to deviate from any type of repeatable pattern. Based on the facts mentioned earlier it becomes clear that it is this irregular high frequency and/or amplitude of the central vortex coupled with the break off of the flow around the central portion of the lower block that triggers the transition to turbulent flow. It should be noted that for Rayleigh numbers larger than 9×10^5, despite using a highly vectorized and efficient algorithm, the required computational time for obtaining accurate results becomes increasingly prohibitive. This increase in computational time is expected since even for $Ra = 9 \times 10^5$ we are already observing some chaotic features, i.e. very high frequencies for the central vortex's movements and the apparent lack of any persistent pattern, in the flow field. Therefore, for $Ra \geqslant 9 \times 10^5$ we must in essence perform direct turbulent flow simulations. Obviously, such a task calls for the use of much finer grid resolutions and the use of much smaller time steps resulting in a very large increase in the computational time. The presence of turbulence for Rayleigh numbers greater than 10^7 was checked through some simple experimental runs (see the Appendix).

All the oscillations which were mentioned earlier from $Ra \geqslant 3 \times 10^5$ to $Ra < 9 \times 10^5$ followed a regular pattern and they were physically induced. In each case it was ascertained that using larger spatial extensions or smaller time steps (relative to what was used to obtain the numerical results) have no influence on the transient as well as the steady or the oscillatory state results for the stream function, temperature, vorticity

and the temporal Nusselt number distributions. This was done in three stages. First, we tested the effect of a spatial domain extension by increasing the size of the open-ended region. For example, for a case where the numerical runs were obtained for a computational domain which had been extended by N times the cavity height, the spatial domain would be sequentially extended to $(N+A)$ times and then to $(N+A+B)$ times the cavity height in each direction. The value for A was usually chosen somewhere from 12 to 20 and the value for B was mostly taken as 20 but never below 12.

Next, we used two different time step sizes which were respectively half and one fourth of the time step size for which the numerical runs were obtained. The latter process during the second stage was done with the proper extensions found from the first stage of our accuracy tests. For example, if we had found during the first stage of our tests that using extensions beyond N times the cavity height had no effect on our results, we would then apply the second stage of our tests for an N times the cavity height extended computational domain. This way we could isolate the spatial and time step size effects on the results. If a discrepancy was observed at any time during the first couple of stages, the test procedure sequence would be interrupted at that point. We would then either increase the domain extension or decrease the computational time step or both (depending on the results of the tests from the first and the second stages) and then restart the entire test procedure. We would continue the above-mentioned procedure until we would observe no changes in our results during the first and second stages of our test procedure.

The above-mentioned procedures constituted the first and second stages of our test procedure. Having established there would be no changes in our results from the increases in the spatial domain and reductions in the computational time step we would then move into the third stage of our checks. For the third stage we would adopt the largest of the spatial extensions, and the smallest of the computational time steps which were used in the first and second stages. The third stage enabled us to ensure that the simultaneous changes in the spatial domain and the time steps had no influence on any of our results. However, it should be noted we never obtained any information from the third stage which was additional (or in conflict) to what was already obtained in the first and the second stages. For example, if we had learned through the first and second stages that:

(1) using any additional extension beyond N times the cavity height had no effect on our results;

(2) and that also using the N times the cavity height extension; reducing computational time steps beyond Δt does not have any effect on the results;

we would then always observe that simultaneously increasing the number of cavity height extensions more than N and reducing the time step beyond Δt will have no effect on our results. It was also found that using the proper number of extensions and the time step size found at a higher Rayleigh number could obviously be used for computational runs at a lower Rayleigh number.

We also tested the effects of using a larger number of grid points for a chosen spatial domain. However, again we never observed an influence from an increase in the number of grid points. This was expected, since at all times we are using a fine and judiciously distributed variable grid structure with special concentration on the critical regions in the flow field. It should be mentioned that these tests were also carried out for the lower range of the Rayleigh numbers as well and not just for Rayleigh numbers for which oscillatory flow was observed. However, as expected the tests for Rayleigh numbers which did lead to an oscillatory flow were more demanding from a computational point of view. As a final check after determining the suitable extension for the computational domain and the size of the computational time increment (and using these values) we doubled (in some cases we increased the total simulation time even further) the total simulation time for the program to see if we will observe any differences in our transient, steady or oscillatory state results. Again, as expected, we never observed an influence from an increase in the total simulation time while using the computational extension and time increments which were determined from our three stage test procedures.

A sample representation of some test runs for Rayleigh numbers in the range of $2\times10^5 \leqslant Ra \leqslant 8\times10^5$, is summarized in Table 2. Specifically some test results for $Ra = 2\times10^5$, 3×10^5, 5×10^5, 6×10^5, and 8×10^5 with the essence of conclusions which have been based on the figures corresponding to these test results are given in this table. It should be noted that all the comments given in Table 2 essentially pertain to the steady state or the oscillatory state of the transient solutions. For example, as it can be seen from Table 2 for cases 1 and 2, for $Ra = 2\times10^5$ using a 32 times the cavity height extension is just not enough despite of the size of the computational time increment, Δt. It should be noted that at $Ra = 2\times10^5$ even for a 32 times the cavity height extension, the solution diverges. If we increase the extent of the computational domain to 48 times the cavity height while keeping the same Δt which was used in case 1, a solution which displays an oscillatory behavior is observed (case 3 in Table 2). Keeping the same computational domain as in case 3 while decreasing the size of the computational time increment Δt (case 4) will lead to a steady state solution with no oscillatory behavior. An attentive study of cases 3–7 (in Table 2) will show that the suitable number of cavity height extensions and the Δt for $Ra = 2\times10^5$ are 48 and 10^{-3}, respectively.

It is interesting to note the points that were made earlier with respect to the redundancy of stage 3 of our tests and our final check on the total simulation

Table 2. Information related to the effects of the outer boundary and convergence and accuracy analysis

Case No.	*Ra*	Number of extensions	Time increment	Total time	Comments
1	200 000	32	1/600	600	Diverged
2	200 000	32	1/1000	1000	Diverged
3	200 000	48	1/600	600	Oscillation
4	200 000	48	1/1000	1000	Converged to a steady state solution; no oscillation
5	200 000	60	1/600	600	Oscillation (no difference between cases 3 and 5)
6	200 000	60	1/1000	1000	Converged to a steady state solution; no oscillation
7	200 000	60	1/5000	4350	Converged to a steady state solution; no oscillation; no difference between cases 4, 6 and 7
8	300 000	60	1/5000	2000	Oscillation (case 8 differs very little from cases 9 and 10)
9	300 000	60	1/10 000	5000	Oscillation (refined)
10	300 000	60	1/20 000	10 000	Oscillation (refined; no difference between cases 9 and 10)
11	500 000	2	1/10 000	5000	Diverged
12	500 000	8	1/10 000	5000	Diverged
13	500 000	16	1/10 000	10 000	Diverged
14	500 000	32	1/10 000	5000	Irregular oscillation
15	500 000	48	1/10 000	5000	Oscillation (case 15 differs very little from cases 16 to 21)
16	500 000	60	1/10 000	5000	Oscillation (refined)
17	500 000	60	1/10 000	10 000	Oscillation (refined)
18	500 000	60	1/20 000	10 000	Oscillation (refined)
19	500 000	60	1/40 000	20 000	Oscillation (refined)
20	500 000	80	1/10 000	5000	Oscillation (refined)
21	500 000	80	1/10 000	10 000	Oscillation (refined; no difference between cases 16 and 21)
22	600 000	60	1/10 000	5000	*W* shape
23	600 000	60	1/20 000	10 000	*W* shape (refined)
24	600 000	80	1/10 000	5000	*W* shape (no difference between cases 22 and 24)
25	600 000	80	1/20 000	10 000	*W* shape (refined; no difference between cases 23 and 25)
26	800 000	60	1/10 000	5000	*W* shape
27	800 000	60	1/20 000	10 000	*W* shape (refined)
28	800 000	60	1/40 000	20 000	*W* shape (refined)
29	800 000	80	1/20 000	10 000	*W* shape (refined; no difference between cases 27 and 29)

time. For example, as seen from the specs on cases 3 and 5 one can draw the conclusion that extending the computational domain by 48 times the height of the cavity is a suitable extension even before seeing the results of cases 6 and 7. But, just to rigorously prove this somewhat intuitive conclusion we continued on running these additional tests. The conclusions and comments with respect to $Ra = 3 \times 10^5$ are quite self-evident, i.e. the number of extensions and Δt are 60 and 10^{-4}, respectively. Again, Table 2 includes just a sample presentation of some of the tests for only some of the Rayleigh numbers which were researched in our work. For $Ra = 5 \times 10^5$, most of the stream function and the temperature contours are also presented. A comparison of these plots and the specs for cases 11–21 makes our earlier statement with respect to the inadequacy of *a maximum of two times the cavity height extension used by the previous investigators* amply clear. The suitable number of extensions and Δt for this case turn out to be 60 and 10^{-4}, respectively. The nature of the asymmetric sinusoidal oscillations which were discussed earlier can be studied in more detail from this table. As it can be clearly seen once a suitable number of extensions and the size of computational time increment are determined from our tests the occurrence, frequency and amplitude of oscillations will be independent of an increase in the number of the extensions and/or a decrease in the computational time increment and/or an increase in the total simulation time.

Based on the results for $Ra = 6 \times 10^5$ (cases 22–25 and the related figures which were analyzed for Table 2) it becomes clear that a suitable number of extensions and Δt are respectively 60 and 5×10^{-5}. Again, as it was noted for earlier cases, by just studying the results of cases 22 and 24 it can be concluded that extending the computational domain by 60 times the cavity height is enough for $Ra = 6 \times 10^5$. The comments which were made with respect to the nature of oscillations for $Ra = 5 \times 10^5$ equally apply for the distorted *W* shape oscillations observed in the range of $6 \times 10^5 \leqslant Ra < 9 \times 10^5$.

A global accuracy check was done on the problem by using the overall energy balance. Assuming the temperature gradients and the excess temperatures (above the ambient temperature) around the periphery of the computational domain are exactly equal to zero and integrating the energy equation from $t = 0$ to $t_{\text{steady state}}$ results in the following approximate global energy balance:

$$Q_{\text{total}} = [\Delta U] = U_{\text{steady state}} - U_{\text{initial state}}. \quad (4)$$

In the above expression Q_{total} refers to the total energy which has been transferred from both of the two heated blocks into the computational domain from $t = 0$ to $t_{\text{steady state}}$, and $U_{\text{steady state}}$ and $U_{\text{initial state}}$ refer to

the internal energy of the computational domain at the steady and initial states, respectively. With respect to the assumptions which have been used in developing equation (4), first it should be noted that our computational domain is extended far enough such that the temperature gradients around the periphery of the computational domain are almost zero. However, although the excess temperatures around the periphery of the computational domain have mostly died down, they are not exactly equal to zero (in our numerical simulations the exact values for the excess temperature around the periphery of the computational domain are computed). Therefore, as it was noted earlier equation (4) does not constitute an exact global check on our numerical results. With this in mind, it was found that the values of the left-hand side and the right-hand side of equation (4) differ by not more than 1.2%. For example, for the case of $Ra = 10^5$, $A = 1/2$, $\theta_2 = 1$, and $Pr = 0.71$ the value of Q_{total} was 335.5 J per unit depth of the cavity while the value of $[\Delta U]$ turned out to be 339.0 J per unit depth of the cavity. The procedures which have been described in the earlier part of this section constitute more precise, detailed and thorough numerical accuracy and convergence tests. Comparisons were also made with the work of Chan and Tien [4] for their geometry and the boundary conditions that they used for $Ra \leqslant 10^8$. The maximum difference between the two sets of results was found to be 3%.

4. ANALYSIS OF THE FREQUENCY OF OSCILLATIONS OF THE CENTRAL VORTEX INSIDE THE CAVITY AND ITS RELATION WITH THE NUSSELT NUMBER

The results of each of the runs for $Ra = 3\times10^5$, 3.5×10^5, 4×10^5, 4.5×10^5, 5×10^5, 5.5×10^5, 6×10^5, 6.5×10^5, 7×10^5, 7.5×10^5, and 8×10^5 were checked in great detail to determine precisely the frequency of the Nusselt number oscillations. The locations and the values (directly from the generated numerical data and not the figures) of the maximum and minimum (local and absolute) and some intermediate values of the Nusselt numbers including the corresponding values of the maximum stream function, $\psi_{\max}$, the maximum and minimum values of the vorticity, $\xi_{\max}$ and $\xi_{\min}$, and the non-dimensional time, t, at those locations were carefully recorded (during the oscillatory phase) and analyzed for all the above-mentioned Rayleigh numbers. It should be mentioned that all these quantities were recorded for each of the above-mentioned Rayleigh numbers for many cycles during the oscillatory phase. This analysis generated several, interesting results. For example it was established that these oscillations essentially start from $Ra \geqslant 3\times10^5$. From $3.5\times10^5 \leqslant Ra \leqslant 5.5\times10^5$, the oscillations are in the shape of asymmetric sinusoidal waves. For values of $Ra \geqslant 6\times10^5$, these sinusoidal oscillations in the Nusselt number distribution will no longer exist. For Rayleigh numbers larger than $Ra = 6\times10^5$, the sinusoidal oscillations are converted to distorted W shaped oscillations. These latter patterns of oscillations in the temporal Nusselt number distribution will persist from $Ra \geqslant 6\times10^5$ to $Ra < 9\times10^5$. Finally, for $Ra \geqslant 9\times10^5$ the W shaped pattern breaks down to some intermediary W's and at the same time part of the flow separates and breaks off from the central part of the lower block. Furthermore, on the basis of several numerical experiments it becomes clear that, for cases in which $Ra \geqslant 9\times10^5$, the central vortex's oscillation frequency becomes much higher and it starts to deviate from any type of repeatable pattern.

A sample presentation of some data and figures which were used in the above-mentioned analysis for $Ra = 5\times10^5$ and 6×10^5 are given in Tables 3 and 4 and the related Figs. 3–11. The results presented for $Ra = 5\times10^5$ are representative of the nature of the asymmetrical sinusoidal oscillations which occur within the range of $3\times10^5 \leqslant Ra \leqslant 5.5\times10^5$ and the results presented for $Ra = 6\times10^5$ represent the nature of the distorted W oscillations which happen within the range of $Ra \geqslant 5.5\times10^5$ to $Ra < 9\times10^5$. The correlation between locations 1–8 listed in Table 3 and its related figures and the Nusselt number oscillations are given in Fig. 12(a). Likewise, the correlation between locations 1–16 listed in Table 4 and its related figures and the Nusselt number oscillations are given in Fig. 12(b). Figures 12(a) and (b) each show two consecutive cycles for the asymmetric sinusoidal and the distorted W oscillations in the temporal Nusselt number distributions. Points 1–4 are the locations on the first asymmetrical sinusoidal cycle and the points 5–8 are the locations on the next (second) cycle shown in Fig. 12(a). Similarly, points 1–8 are the locations on the first distorted W cycle and the points 9–16 are the locations on the subsequent (second) cycle shown in Fig. 12(b).

The presence of a very regular and one to one pattern and relationship between the frequency of oscillations in the Nusselt number and the central vortex's location and oscillation inside the cavity becomes quite apparent from the results presented in Tables 3 and 4 and the related figures corresponding to these tables. The linear relationship between the frequency of the oscillation of the central vortex in the cavity, Ω, and the Rayleigh number was found to be

$$\Omega(Ra) = \alpha\, Ra + \beta \tag{5}$$

where

$\alpha = 1.02\times10^{-4}$ and $\beta = 47$

for $3.5\times10^5 \leqslant Ra \leqslant 5.5\times10^5$

and

$\alpha = 4.27\times10^{-5}$ and $\beta = 28.9$

for $6\times10^5 < Ra \leqslant 8\times10^5$.

This linear relationship is displayed in Fig. 13. The figures related to Tables 3 and 4 provide a very clear

Table 3. Information related to vortex oscillations presented in Figs. 3–5

Location	Non-dimensional time	ψ_{max}	ξ_{min}	ξ_{max}	Related figure
1	0.2622	−106.2	−10870	1839	3;5
2	0.2643	−114.5	−10438	2005	3;5
3	0.2662	−113.3	−10304	2420	3;5
4	0.269	−102.6	−9900	2304	3;5
5	0.2723	−105.9	−10876	1839	4;5
6	0.2744	−114	−10476	2012	4;5
7	0.2763	−112.9	−10292	2451	4;5
8	0.2791	−102.5	−9933	2315	4;5

Table 4. Information related to vortex oscillations on heat transfer displayed in Figs. 6–11

Location	Non-dimensional time	ψ_{max}	ξ_{min}	ξ_{max}	Related figure
1	0.2591	−126.26	−11495	2772	6;10
2	0.2615	−112.96	−11199	2711	6;10
3	0.2639	−109.49	−11306	2137	6;10
4	0.26595	−117.55	−11596	2094	6;10
5	0.268	−120.23	−11539	2570	7;10
6	0.27115	−108.8	−10463	2314	7;10
7	0.27425	−117.54	−12345	2183	7;10
8	0.2759	−126.7	−11718	2357	7;10
9	0.2775	−125.5	−11480	2786	8;11
10	0.2799	−112.29	−11166	2702	8;11
11	0.2823	−109.33	−11382	2112	8;11
12	0.28435	−117.28	−11594	2104	8;11
13	0.2864	−119.82	−11541	2574	9;11
14	0.2895	−108.45	−10516	2327	9;11
15	0.2926	−116.87	−12326	2175	9;11
16	0.29425	−126.06	−11727	2316	9;11

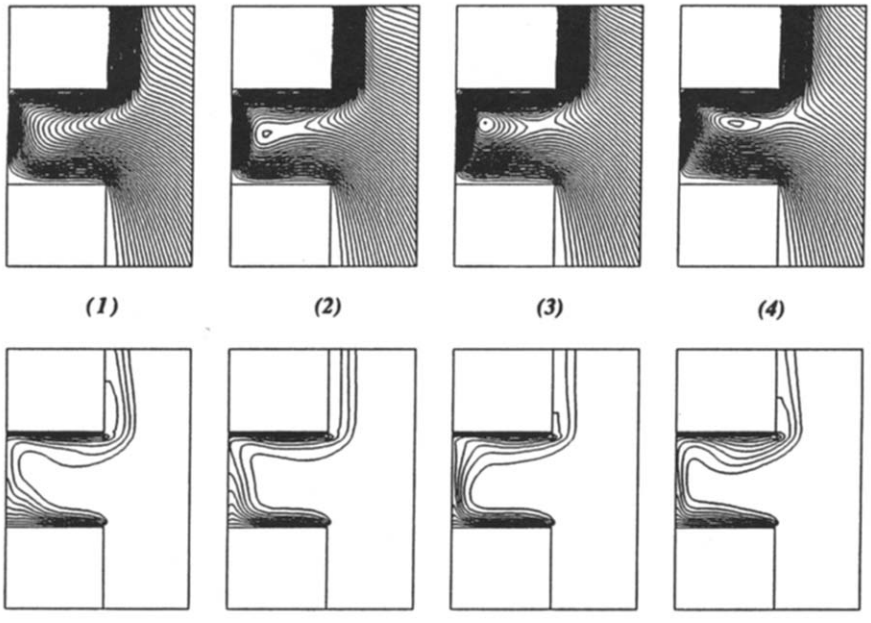

FIG. 3. The location of the central vortex and the temperature contours for $\theta_2 = 1$, $A = 0.5$, $Pr = 0.71$, $Ra = 5 \times 10^5$ and for locations 1–4 given in Table 3 and displayed in Fig. 12(a).

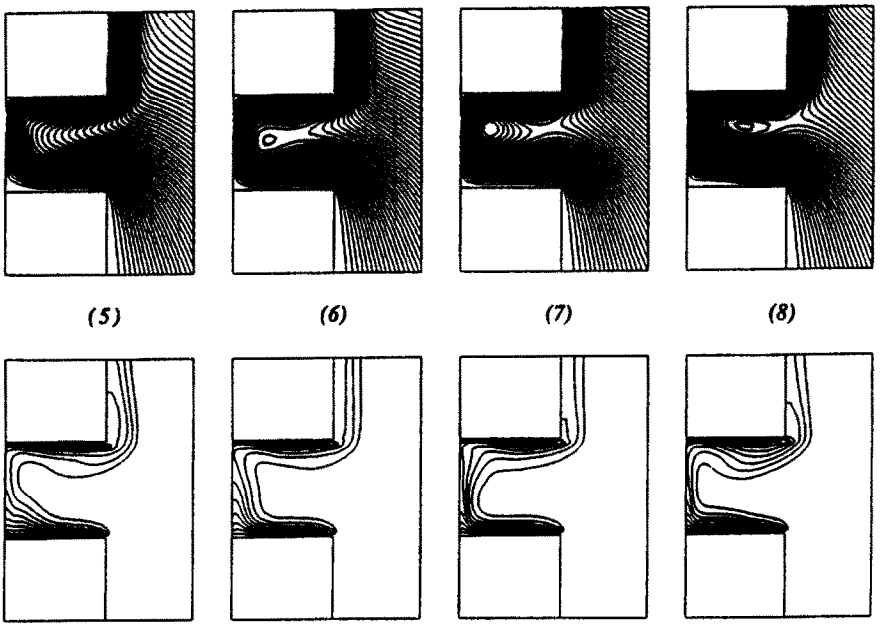

FIG. 4. The location of the central vortex and the temperature contours for $\theta_2 = 1$, $A = 0.5$, $Pr = 0.71$, $Ra = 5 \times 10^5$ and for locations 5–8 given in Table 3 and displayed in Fig. 12(a).

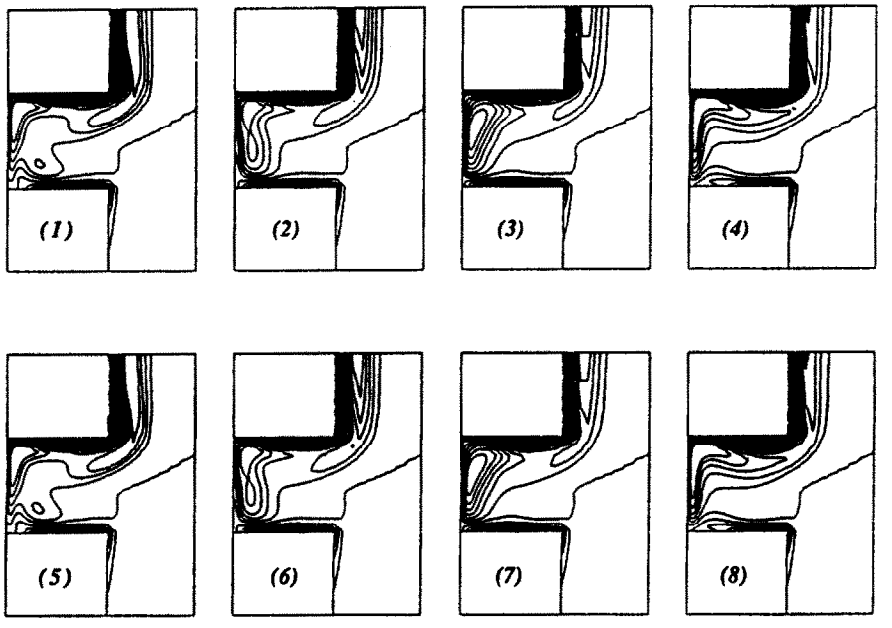

FIG. 5. Vorticity contours corresponding to the streamlines and isotherms displayed in Figs. 3 and 4.

picture of the vorticity field and its interaction with the movement of the central vortex inside the cavity. These set of contours also clearly show that each oscillation cycle is very repeatable. If we were to compare the stream function, the temperature and vorticity contours for the set of locations 1–4 corresponding to the first cycle of the asymmetrical sinusoidal oscillations, with the corresponding contours for the set of locations 5–8 corresponding to the second cycle of these oscillations we would be hard pressed to find any differences. For higher Rayleigh numbers, $Ra > 550\,000$ to $Ra < 900\,000$, while the oscillation pattern does become more complex, it is still very regular and repetitious. Therefore, again the same conclusions which were stated for the asymmetrical oscillations can be stated about the contours

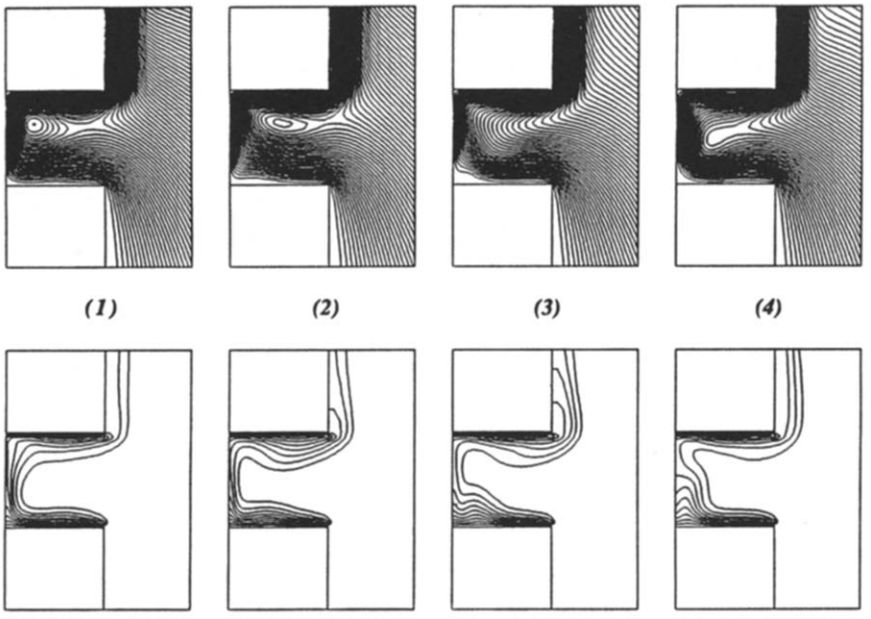

FIG. 6. The location of the central vortex and the temperature contours for $\theta_2 = 1$, $A = 0.5$, $Pr = 0.71$, $Ra = 6 \times 10^5$ and for locations 1–4 given in Table 4 and displayed in Fig. 12(b).

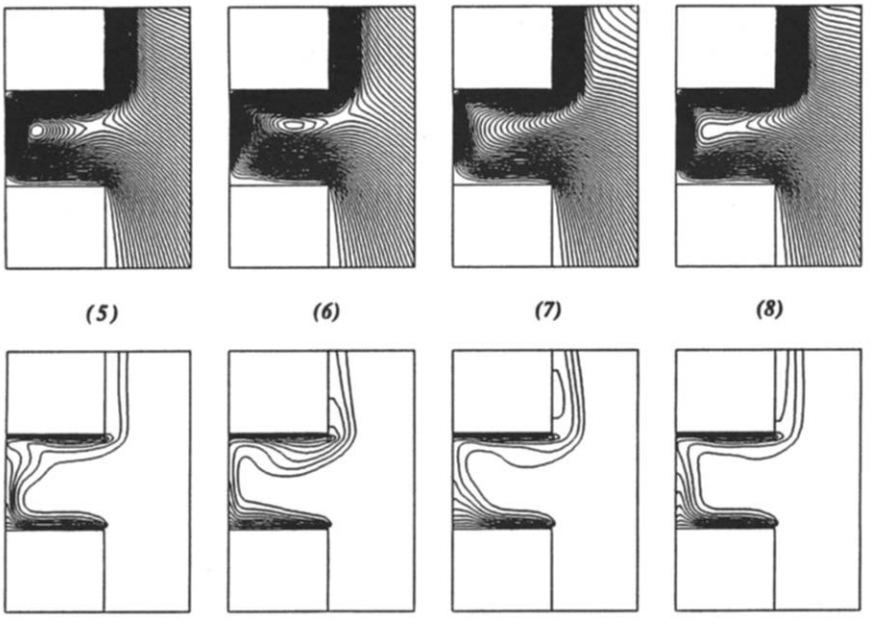

FIG. 7. The location of the central vortex and the temperature contours for $\theta_2 = 1$, $A = 0.5$, $Pr = 0.71$, $Ra = 6 \times 10^5$ and for locations 5–8 given in Table 4 and displayed in Fig. 12(b).

for the set of locations 1–8 corresponding to the first cycle of the W oscillations and the contours for the set of locations 9–16 corresponding to the second cycle of these oscillations. Overall the set of contours related to Tables 3 and 4 provide a vivid description of the movement of the central vortex inside the cavity and its interaction with the temperature and vorticity fields.

The patterns mentioned earlier are even more regular than what has been presented in Tables 3 and 4 and the related figures. This is because the values of maximum and minimum Nusselt numbers are very slightly dependent on the finite size of the time step, Δt, used in the numerical calculations. That is the cut-off point where the maximum or the minimum values of the Nusselt numbers are selected are generally

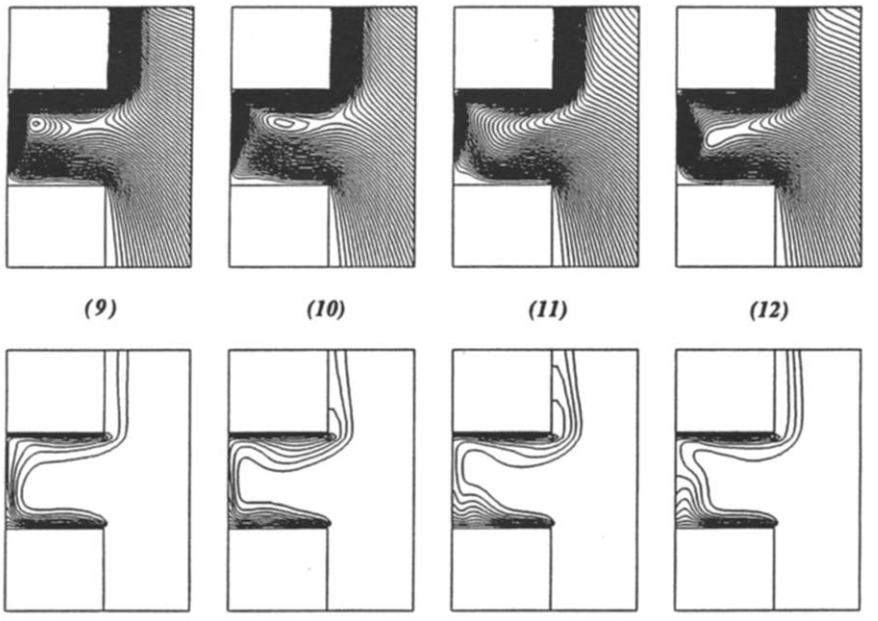

FIG. 8. The location of the central vortex and the temperature contours for $\theta_2 = 1$, $A = 0.5$, $Pr = 0.71$, $Ra = 6 \times 10^5$ and for locations 9–12 given in Table 4 and displayed in Fig. 12(b).

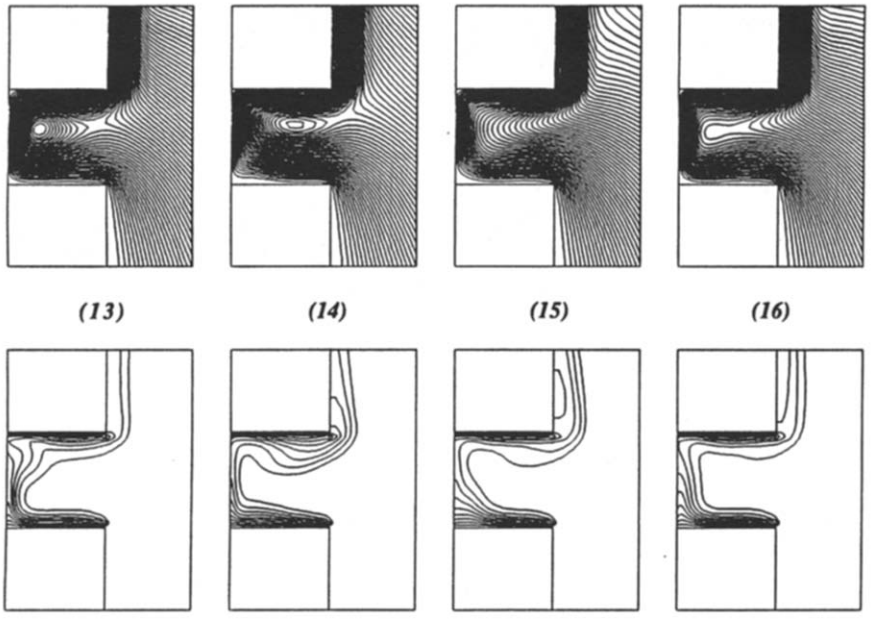

FIG. 9. The location of the central vortex and the temperature contours for $\theta_2 = 1$, $A = 0.5$, $Pr = 0.71$, $Ra = 6 \times 10^5$ and for locations 13–16 given in Table 4 and displayed in Fig. 12(b).

within $\Delta t/2$ of the actual maxima values. The above-mentioned points are a direct consequence of working in a discrete (computational) domain rather than a physical domain. It should be noted, though that the resulting inaccuracy (which is *unavoidable* in any numerical scheme) is very small. In fact, for flow, temperature and vorticity fields as well as the temporal Nusselt number distributions this effect was virtually undetectable.

5. CONCLUSIONS

A number of interesting results with respect to the interrelationship between Nusselt number oscilla-

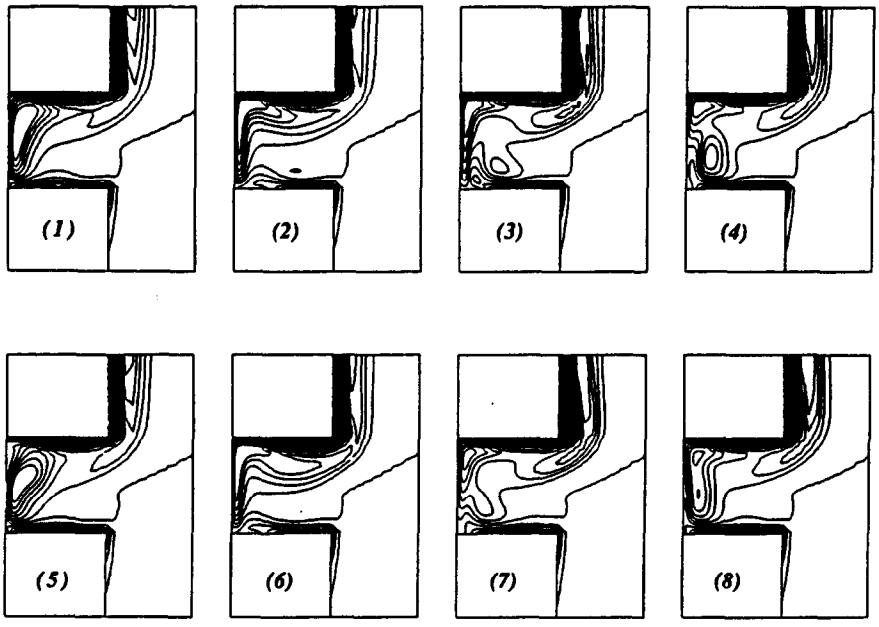

FIG. 10. Vorticity contours corresponding to the streamlines and isotherms displayed in Figs. 6 and 7.

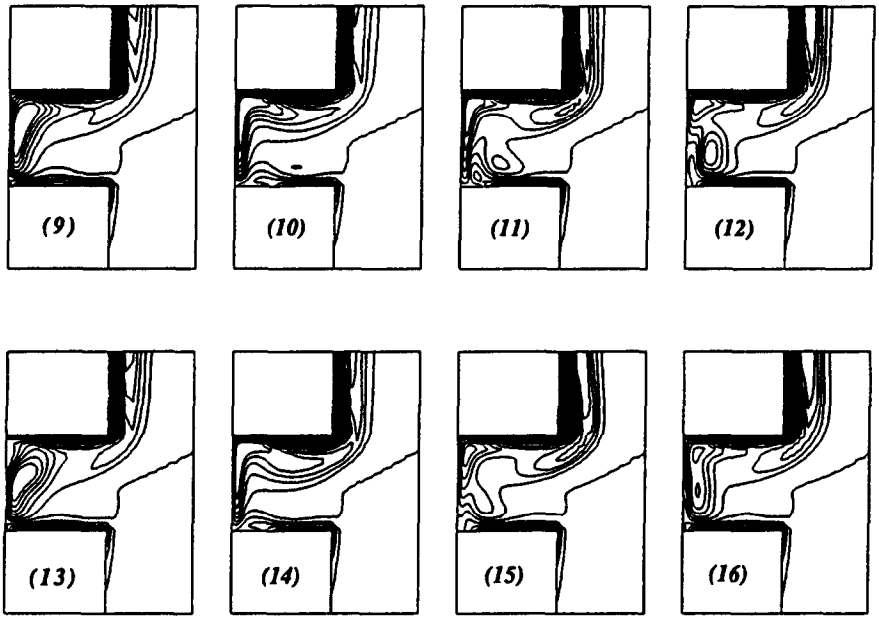

FIG. 11. Vorticity contours corresponding to the streamlines and isotherms displayed in Figs. 8 and 9.

tions, the corresponding temperature distribution, the fluid flow pattern and the vortex dynamics were established in this work. Some of the more pertinent conclusions for buoyancy-driven convection in open-ended cavities are given below.

(1) It was established that the periodic oscillations in the Nusselt number are directly the result of oscillations of the central vortex inside the cavity. In fact, it was established that the frequency of the oscillations for the Nusselt number and the central vortex inside the cavity is the same.

(2) Within the range of $3 \times 10^5 \leqslant Ra < 9 \times 10^5$ two distinct, oscillatory patterns were established. These were: asymmetric sinusoidal and distorted W shaped oscillations. The first pattern existed within $3.5 \times 10^5 \leqslant Ra \leqslant 5.5 \times 10^5$, while the second pattern existed from $Ra \geqslant 6 \times 10^5$ to $Ra < 9 \times 10^5$.

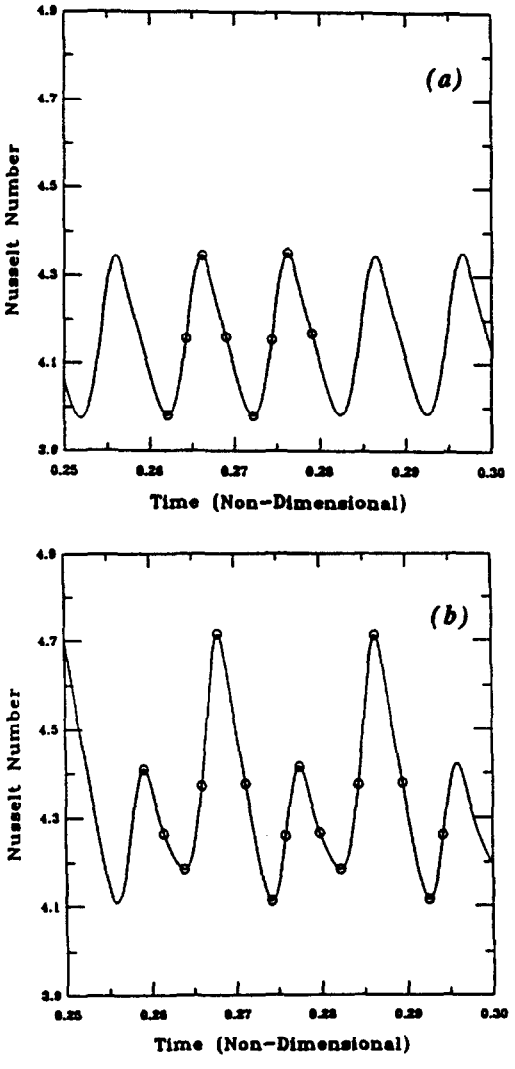

FIG. 12. (a) Correlation between locations 1–8 listed in Table 3 and the vortex oscillations displayed in Figs. 3–5. (b) Correlation between locations 1–16 listed in Table 4 and the vortex oscillations displayed in Figs. 6–11.

(3) The frequency of the oscillations of the central vortex inside the cavity (or the Nusselt number) during the oscillatory phase was found to be directly related to the Rayleigh number. The relationship between the frequency of oscillation of the central vortex in the cavity, Ω, and the Rayleigh number was found to be

$$\Omega(Ra) = \alpha\, Ra + \beta$$

where

$$\alpha = 1.02 \times 10^{-4} \quad \text{and} \quad \beta = 47$$

$$\text{for} \quad 3.5 \times 10^5 \leqslant Ra \leqslant 5.5 \times 10^5$$

and

$$\alpha = 4.27 \times 10^{-5} \quad \text{and} \quad \beta = 28.9$$

$$\text{for} \quad 6 \times 10^5 < Ra \leqslant 8 \times 10^5.$$

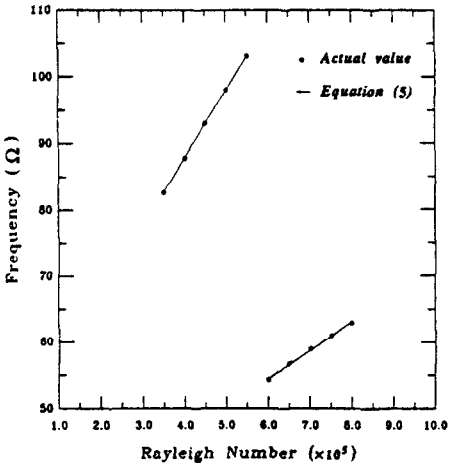

FIG. 13. Frequency of the oscillation of the central vortex inside the cavity, Ω, as a function of the Rayleigh number, Ra.

(4) In every instance, the frequency and the amplitude of the oscillations during the oscillatory phase were extremely regular in pattern, magnitude, etc.

(5) A relationship between the Nusselt number oscillations and the onset and prediction of turbulence was shown to exist.

REFERENCES

1. M. L. Doria, A numerical model for the prediction of two-dimensional unsteady flows of multi-component gases with strong buoyancy effects and recirculation, Notre Dame Report, TR-37191-74-4 (1974).
2. H. R. Jacobs, W. E. Mason and W. T. Hikida, Natural convection in open rectangular cavities, *Proc. Fifth Int. Heat Transfer Conf.*, Tokyo, Japan, Vol. 3, pp. 90–94 (1974).
3. H. R. Jacobs and W. E. Mason, Natural convection in open rectangular cavities with adiabatic sidewalls, *Proc. 1976 Heat Transfer and Fluid Mech. Inst.*, pp. 33–46. Stanford University Press, Standford (1976).
4. Y. L. Chan and C. L. Tien, A numerical study of two-dimensional natural convection in square open cavities, *Numer. Heat Transfer* **8**, 65–80 (1985).
5. Y. L. Chan and C. L. Tien, Laminar natural convection in shallow open cavities, *21st ASME–AIChE Natn. Heat Transfer Conf., Natural Convection in Enclosures—1983*, HTD Vol. 26, pp. 77–82 (1983).
6. K. S. Chen, J. A. C. Humphrey and F. S. Sherman, Experimental investigation of thermally driven flow in open cavities of rectangular cross-section, *Phil. Trans. R. Soc. London* **A316**, 57–84 (1985).
7. V. Sernas and I. Kyriakides, Natural convection in an open cavity, *Proc. Seventh Int. Heat Transfer Conf.*, Munchen, Germany, Vol. 2, pp. 275–286 (1982).
8. F. Penot, Numerical calculation of two-dimensional natural convection in isothermal open cavities, *Numer. Heat Transfer* **5**, 421–437 (1982).
9. J. Adams and J. Ortega, A multicolor SOR method for parallel computation, *Proc. Int. Conf. on Parallel Processing*, pp. 53–56 (1982).
10. P. J. Roache, *Computational Fluid Dynamics*. Hermosa, Albuquerque (1976).

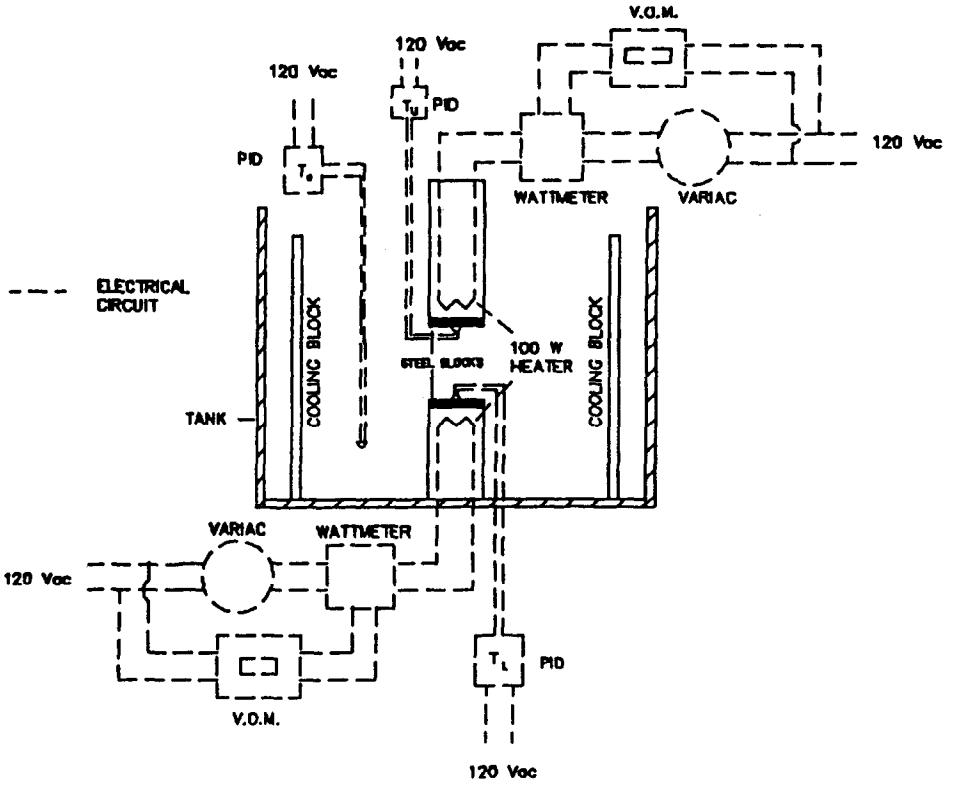

FIG. A1. Schematic of the experimental set-up.

11. K. Vafai and J. Ettefagh, The effects of sharp corners on buoyancy-driven flows with particular emphasis on outer boundaries, *Int. J. Heat Mass Transfer* **33**, 2311–2328 (1990).
12. J. Ettefagh and K. Vafai, Natural convection in open-ended cavities with a porous obstructing medium, *Int. J. Heat Mass Transfer* **31**, 673–693 (1988).

APPENDIX

The experimental apparatus described below was used to provide a crude, visual check on the use of the symmetry conditions at the centerline of the open-ended cavity. The rigorous and precise examination of the use of the symmetry conditions was done through extensive and systematic numerical experimentation. The apparatus depicted in Fig. A1 consisted of a water tank, cooling plates, and couple of heating units. The tank ($22 \times 12 \times 6.5$ in.) was constructed of 0.5 in. plexiglas so that, we could maintain relatively easy optical access to the test section. The far field ambient conditions were simulated by using a hollow (to allow for the circulation of the coolant fluid) cooling plate ($12 \times 6.5 \times 0.75$ in.) made of aluminum on each end of the water tank. Each of the heated blocks were simulated by using a narrow strip heater with a steel block with the same base dimensions and 1.5 in. thickness cemented on top of the strip heater. Referring to Fig. 1, the strip heater was chosen so that, it would be much longer in the z-direction than the x-direction to reduce the end effects. Each of the strip heater units (the strip heater and the steel block) was placed within a box built from balsa wood. The box, the heater and the steel plate were all cemented using waterproof epoxy glue and the electrical connections were sealed by using a silicon based sealer. The back side of the heaters and all the side walls of the boxes which contained the heating units were insulated with fiberglass insulation.

The input power to the heaters was controlled by two independently controlled PID (proportional integral differential) temperature controllers. These controllers used the feedback from the thermocouples which were mounted on the surfaces of the heating units to maintain a constant temperature condition on those surfaces. The flow field visualization was done through injecting dye into the water tank. Since the working fluid was water, the lowest achievable Rayleigh number was $Ra = 5 \times 10^6$. The flow field patterns were explored in the range of $5 \times 10^6 \leqslant Ra \leqslant 10^7$. Based on our observations, the flow field appeared to be symmetric around $Ra = 5 \times 10^6$ with respect to the mid-plane of the open-ended cavity. That is we did not observe movement of the dye across the mid-plane of the cavity. Furthermore, based on our observations we were also able to observe the presence of certain turbulent features around $Ra = 10^7$.

INSTABILITES COUPLEES THERMIQUES ET DYNAMIQUES DANS DES ECOULEMENTS FLOTTANTS DANS DES CAVITES OUVERTES

Résumé—Les configurations de la convection naturelle dans une cavité ouverte sont analysées et une présentation détaillée des résultats est donnée. On montre qu'aux nombres de Rayleigh les plus forts, il existe une relation univoque entre la fréquence des oscillations périodiques du nombre de Nusselt et les oscillations du tourbillon central et la position dans la cavité. En fait, pour un type donné quelconque d'oscillation (par exemple, sinusoïdal asymétrique ou W distordu), la fréquence des oscillations du nombre de Nusselt (ou du tourbillon central dans la cavité) augmente linéairement quand le nombre de Rayleigh croît. Pour l'air, cette relation linéaire est explicitée. On constate que pour des cas où $Ra \geqslant 9 \times 10^5$, la fréquence d'oscillation du tourbillon central devient beaucoup plus grande et elle commence à dévier de n'importe quel type de configuration reproductible. On propose que c'est ce mouvement irrégulier à haute fréquence du tourbillon central, couplé à la séparation de l'écoulement autour de la section moyenne du bloc inférieur qui déclanche la transition à l'écoulement turbulent.

GEKOPPELTE THERMISCHE UND STRÖMUNGS-INSTABILITÄTEN IN AUFTRIEBSSTRÖMUNGEN IN NACH OBEN OFFENEN HOHLRÄUMEN

Zusammenfassung—Die Grundlagen der auftriebsgetriebenen Strömung in einem offenen Hohlraum werden analysiert, die Ergebnisse werden ausführlich dargestellt. Es zeigt sich, daß bei hohen Rayleigh-Zahlen das Verhältnis der folgenden Größen eins beträgt: Frequenz der periodischen Schwankungen der Nusselt-Zahl, Frequenz der Schwankungen des Zentralwirbels und Position innerhalb des Hohlraums. Tatsächlich gilt für jeden vorgegebenen Typ der Oszillationsform (z. B. asymmetrisch sinusförmig oder gestört), daß die Frequenz der Schwankungen der Nusselt-Zahl (oder die Frequenz der Schwankungen des Zentralwirbels im Hohlraum) linear mit steigender Rayleigh-Zahl zunimmt. Für Luft wird dieser lineare Zusammenhang explizit bestimmt. Außerdem wird festgestellt, daß bei $Ra \geqslant 9 \times 10^5$ die Frequenz der Schwankungen des Zentralwirbels viel größer wird und von jeglicher reproduzierbarer Form abzuweichen beginnt. Es wird vorgeschlagen, daß der Übergang zur turbulenten Strömung gerade durch diese unregelmäßige hochfrequente Bewegung des Zentralwirbels ausgelöst wird, die mit einer Strömungsablösung im Bereich des Mittelteils der Unterseite gekoppelt ist.

ВЗАИМОСВЯЗАННЫЕ ТЕПЛОВАЯ НЕУСТОЙЧИВОСТЬ И НЕУСТОЙЧИВОСТЬ ТЕЧЕНИЙ, ОБУСЛОВЛЕННЫХ ПОДЪЕМНЫМИ СИЛАМИ, В НЕЗАМКНУТЫХ ПОЛОСТЯХ

Аннотация—Анализируются основные особенности конвекции за счет подъемных сил в незамкнутой полости. Показано, что при высоких значениях числа Рэлея между частотой периодических колебаний числа Нуссельта и пульсациями центрального вихря, а также местом их локализации в полости существует однозначная зависимость. При заданном колебательном режиме (например, при асимметричном синусоидальном или деформированном W-образном) частота колебаний числа Нуссельта (или центрального вихря внутри полости) линейно возрастает с увеличением числа Рэлея) Отмеченная выше линейная зависимость определена в явной форме для воздуха. Установлено также, что для $Ra \geqslant 9 \times 10^5$ частота пульсаций центрального вихря существенно увеличивается и его поведение начинает отклоняться от повторяющегося режима любого типа. Предполагается, что именно это хаотическое высокочастотное движение центрального вихря совместно с отрывом потока вокруг миделевого сечения нижнего блока инициирует переход к турбулентному течению.